INORGANIC CHEMISTRY FRONTIERS

RESEARCH ARTICLE

View Article Online
View Journal | View Issue



Check for updates

Cite this: *Inorg. Chem. Front.*, 2026, **13**, 754

# Halogen-bond induced polar multilayer hybrid perovskites for efficient self-driven X-ray detection

Haotian Wen,[a,b] Minmin Wang,[a,b] Xin Dong,[b] Zhijin Xu,[b] Yaru Geng,[b] Jie Qin,[a,b] Junhua Luo,[b,d] Min Zhang *[a,c,d] and Lina Li *[a,b,d]

Received 16th September 2025,
Accepted 10th November 2025

DOI: 10.1039/d5qi01912e

rsc.li/frontiers-inorganic

Two-dimensional (2D) hybrid perovskites possess remarkable X-ray absorption and outstanding carrier transport properties, showing great application prospects in efficient X-ray detection. However, most 2D hybrid perovskites require an external voltage to achieve X-ray detection, resulting in excessive device power dissipation and pronounced ion migration effects. Thus, it is necessary to develop novel self-driven X-ray detection materials. Here, by alloying iodine-substituted cations I-BA (I-BA = 4-iodobutylammonium) instead of *n*-butylamine cations into $MAPbI_3$ (MA = methylammonium), a 2D triple-layer polar hybrid perovskite $(I\text{-}BA)_2(MA)_2Pb_3I_{10}$ (**1**) is acquired. Due to the introduction of iodine-substituted amines, additional non-covalent I···H hydrogen bonds between organic cations and I···I halogen bonds between cations and inorganic halides are formed, endowing **1** with a polar structure. Notably, **1** delivers a 0.15 V open-circuit photovoltage under X-ray irradiation and features self-driven X-ray detection behavior. Furthermore, **1** shows a high sensitivity of 221.7 μC $Gy^{-1}$ $cm^{-2}$ with a low limit of detection of 16.3 nGy $s^{-1}$. The distinctive characteristics of **1** render it an excellent candidate for self-driven X-ray detection, simultaneously offering valuable guidance for the precise design of advanced X-ray detection materials.

## Introduction

X-ray detectors serve critical functions across multiple essential domains, particularly in medical diagnostics, non-destructive product evaluation, security inspections, and scientific investigations.[1–6] Consequently, developing novel materials for improved X-ray detection continues to be a major focus of global research efforts.[7] Lead halide perovskites have recently gained prominence in direct X-ray detection applications owing to their facile synthesis,[8] strong X-ray attenuation capabilities,[9–11] and superior optoelectronic performance.[12–16] However, the reliance of most detectors on strong electric fields often causes severe ion migration, resulting in unstable performance, increased energy consumption, and bulky circuit configurations.[15,17,18] Therefore, the development of self-driven devices capable of operating without an external bias voltage has attracted growing attention in X-ray detection.[19]

Traditionally, constructing a p–n heterojunction can generate a spontaneous potential gradient, which leads to photo-induced charge separation and drift for self-driven supply.[20–23] However, the complexity of the manufacturing process and interface engineering hinders the large-scale application of this method.[24] Alternatively, introducing chiral organic cations induces the crystallization of the resulting perovskite into a chiral-polar point group, thus naturally endowing the compound with polar characteristics to generate self-driven photodetection. For instance, self-driven circular polarization photodetection with high sensitivity was achieved in $(R\text{-PPA})EAPbBr_4$.[25] Then, Wu *et al.* successfully achieved self-driven X-ray detection in chiral-polar $(R\text{-MPA})_4AgBiI_8$,[26] which holds great promise for self-driven X-ray detectors. Nevertheless, enantiopure chiral organic ammonium cations obtained through asymmetric synthesis and chiral separation are often scarce and expensive. Therefore, self-driven detection materials constructed based on achiral cations are still highly desired. In lead halide perovskites, non-covalent interactions (steric hindrance, π–π interactions, hydrogen bonds, and van der Waals force)[27,28] among organic cations and those (electrostatic interactions, hydrogen bonds, and halogen bonds)[29,30] between cations and inorganic halides influence the physical properties of the crystal. For instance, Liu *et al.* introduced a carboxylic acid group to construct quasi-Ruddlesden–Popper motifs with reduced energy gaps *via* strong O–H···O hydrogen bonds between adjacent spacer cations.[31] In addition, carboxylic acid dimers significantly enhanced structural rigidity, thereby mitigating non-radiative

[a]*College of Chemistry, Fuzhou University, Fuzhou 350116, China*
[b]*State Key Laboratory of Functional Crystals and Devices, Fujian Institute of Research on the Structure of Matter, Chinese Academy of Sciences, Fuzhou, Fujian, 350002, China. E-mail: lilina@fjirsm.ac.cn*
[c]*State Key Laboratory of Structural Chemistry, Fujian Institute of Research on the Structure of Matter, Chinese Academy of Sciences, Fuzhou 350002, China*
[d]*Fujian Science & Technology Innovation Laboratory for Optoelectronic Information of China, Fuzhou, Fujian, 350108, China*

recombination induced by tensile vibrations.[32] The bromine-substituted organic cations were employed to enhance the molecular dipole moment, hindering oxygen atom diffusion and charged ion migration, leading to improved chemical and operational stability.[33] Given that directional non-covalent interactions play a crucial role in guiding the crystal structure,[34] inducing polarity in hybrid perovskites through non-covalent interactions is promising.

Inspired by this, we present a polar trilayered perovskite hybrid, $(I\text{-}BA)_2(MA)_2Pb_3I_{10}$ (**1**, where I-BA = 4-iodobutylammonium and MA = methylammonium), *via* incorporating iodine-replaced organic spacers. The non-covalent I···H hydrogen bonds between organic cations and I···I halogen bonds between cations and inorganic halides lead to **1** crystallization in a polar space group, thus enabling it to present self-driven photodetection. Moreover, the charge transport is enhanced through increasing the layers of the inorganic framework, thereby improving the self-driven photodetection performance. The high-quality single-crystal (SC) device exhibits a large photocurrent on–off ratio ($5.74 \times 10^3$), a high responsivity (35.3 mA $W^{-1}$), and an outstanding detectivity (>$10^{12}$ Jones) at 520 nm without an external bias voltage. Moreover, due to the excellent photo-response and the inorganic framework composed of heavy elements Pb and I, **1** demonstrates excellent self-driven X-ray detection capability, featuring a sensitivity of 221.7 μC $Gy^{-1}$ $cm^{-2}$, and an impressively low limit of detection (LoD) of 16.3 nGy $s^{-1}$. This work develops a strategy of inducing material polarity through haloamine-incorporated enhancement of non-covalent interactions, paving the way for the design of exceptional self-driven X-ray detection materials.

## Experimental

$Pb(Ac)_2$ (2.27 g, 6 mmol) was dissolved in 48% aqueous HI solution (10 mL) by heating to boiling under constant magnetic stirring to give a yellowish solution. Subsequent addition of aminobutanol (0.36 g, 4 mmol) and MA (0.45 g, 4 mmol) to the hot solution formed a yellowish precipitate, which dissolved under stirring to afford a dark yellow solution. Moreover, it was subsequently dissolved by heating the solution to boiling. Finally, black-red crystals were obtained after the solution was cooled to room temperature. Further details regarding the experimental and computational data are available in the SI.

## Results and discussion

In HI solution, $Pb(OAc)_2$ was mixed with 4-aminobutanol and methylamine in stoichiometric ratios.[35] Through a gradual

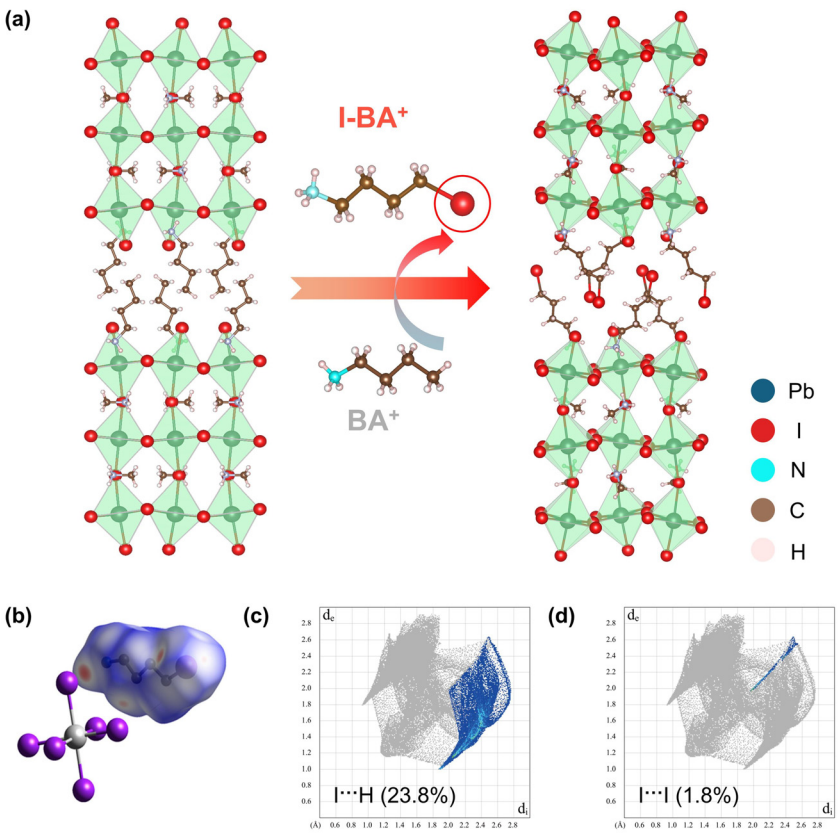


**Fig. 1** (a) The iodine substitution strategy replaces BA cations with I-BA cations. (b) The Hirshfeld surface of I-BA cations in **1**. (c) I···H and (d) I···I interactions.

temperature reduction process, SCs of **1** were successfully grown, and the phase purity was confirmed by comparing the experimental PXRD pattern with the simulated pattern generated from the CIF (Fig. S1, SI). Fig. 1a illustrates the synthesis of **1** through iodine-mediated substitution of BA cations by I-BA cations. The introduction of heavy elements with a large atomic number ($Z$) increases the density to 3.62 g cm$^{-3}$, which is higher than those of two-dimensional hybrid perovskites without halogen-substituted spacers, such as $(BA)_2(MA)_2Pb_3I_{10}$ (3.39 g cm$^{-3}$),[36] $(iBA)_2(MA)_2Pb_3I_{10}$ (3.44 g cm$^{-3}$, where iBA is isobutylamine),[37] and $(PA)_2(MA)_2Pb_3I_{10}$ (3.50 g cm$^{-3}$, where PA is *n*-pentylamine).[38] Such high density is conducive to more efficient absorption of high-energy X-rays.

To further gain in-depth insights into the non-covalent interactions of I-BA cations in perovskites, we analyzed the Hirshfeld dnorm surface plot, 2D fingerprint plot (Fig. 1b–d), and the interactions in **1** using Crystal Explorer software derived from the CIF file. Under the effect of iodine-substituted cations, additional interactions between layers were formed in **1** (Fig. S2 and S3, SI). As a result, the rotational freedom of the bulky cations was reduced to make them orient in an ordered manner, stabilizing **1** in a polar space group *Pc*. Meanwhile, through the point charge model calculation, the value of the electric polarization ($P_s$) along the *c*-axis of **1** was 3.62 μC cm$^{-2}$ (Fig. S4 and Table S1, SI), providing additional verification of its non-centrosymmetric structure (Fig. S5, SI). Considering the polar structure of **1**, it has great potential in self-driven photodetection.

To evaluate the potential of **1** in optoelectronic applications, absorption data for **1** were collected using UV-Vis spectroscopy (Fig. S6, SI). **1** exhibited an absorption edge at approximately 720 nm. By fitting the Tauc's formula, we determined the optical bandgap of **1** to be 1.72 eV. Also, enabled by exceptionally well-formed SCs of **1**, we constructed two-electrode devices with a symmetric Ag/**1** SC/Ag architecture, with Ag electrodes aligned parallel to the polar *c*-axis (Fig. 2a). High resistivity could effectively reduce the current noise and dark current, which is of great significance for exceptional-efficiency X-ray detection. Therefore, by fitting the *I*–*V* curve, a superior resistivity value of 1.45 × 10$^{11}$ Ω cm for single crystal **1** was obtained (Fig. 2b). Fig. S7 depicts the wavelength dependence of the spectral photoresponse. Under the same light power density (2 mW cm$^{-2}$), an excellent photoresponse ($I_{light}$) was obtained at 520 nm. Thus, this wavelength was chosen as the characteristic wavelength for further evaluation of the photodetection performance. Fig. 2c illustrates the current–voltage (*I*–*V*) characteristics measured along the *c*-axis under dark conditions and 520 nm illumination. The symmetry and

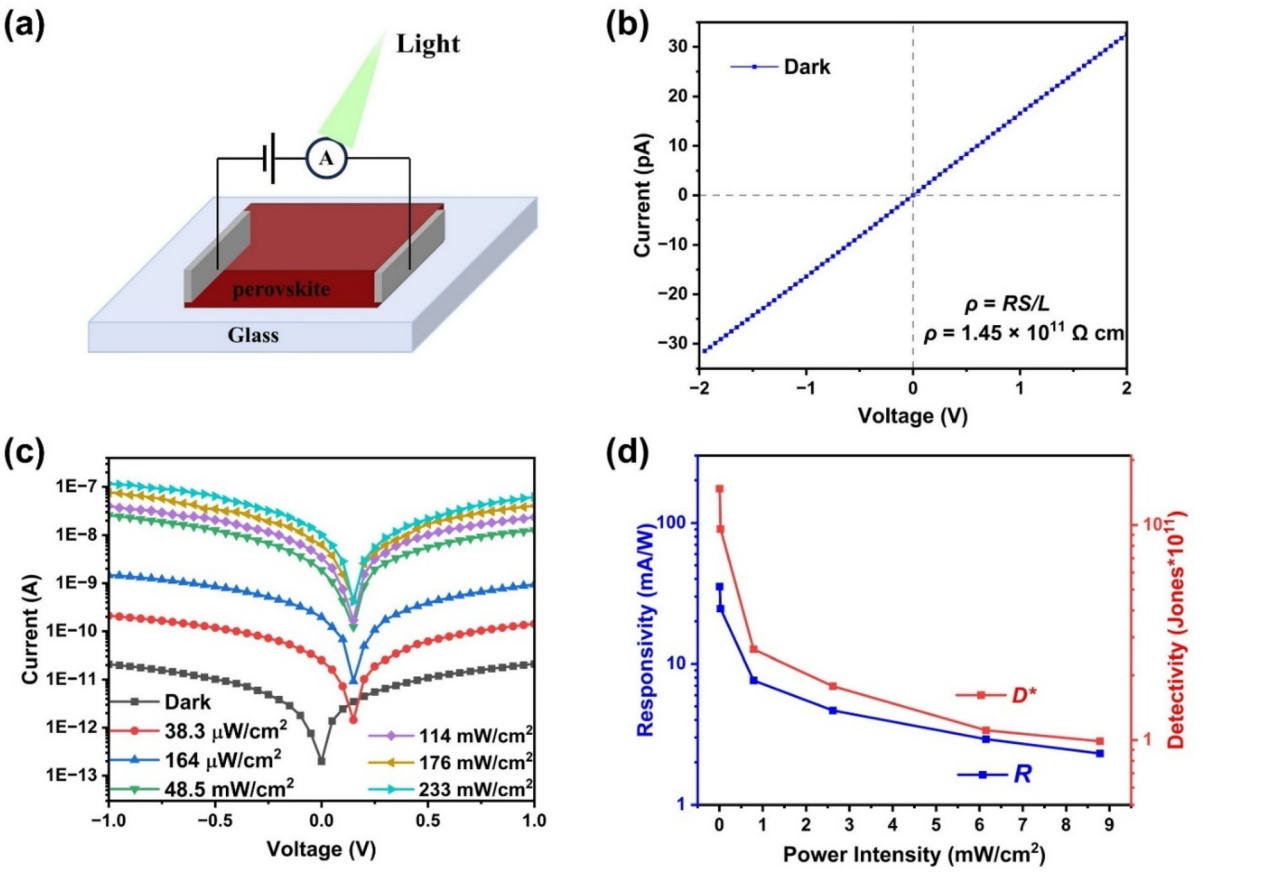


Fig. 2 (a) Device schematic of the lateral two-electrode detection devices constructed with the SC of **1**. (b) The resistivity of **1**. (c) The *I*–*V* curves under 520 nm irradiation. (d) Responsivity and detectivity under 520 nm with different illumination power.

 

linear behavior indicate good ohmic contact between the single crystal and the silver electrodes with a very small contact resistance. In particular, our SC devices exhibited a rather low dark current of approximately 20.9 pA. Such a low value of $I_{dark}$ was highly beneficial for a high detectivity, and the measured corresponding photocurrent ($I_{ph}$) increased rapidly with the increase in light intensity. Under an illumination of 233 mW $cm^{-2}$, the open-circuit photovoltage ($V_{oc}$) was approximately 0.15 V, and the $I_{ph}$ was as high as 0.12 μA. The on/off ratio was calculated to be $5.74 \times 10^3$ (Fig. 2c). Furthermore, the responsivity ($R$) and detectivity ($D^*$), which are important indicators for evaluating the sensitivity of a detector, were calculated to be 35.3 mA $W^{-1}$ and $1.47 \times 10^{12}$ Jones (5.38 μW $cm^{-2}$), respectively (Fig. 2d). These results validate its significant potential in self-driven and highly efficient photodetection applications.

Considering the excellent self-driven photoelectric detection performance in the visible light range, combined with the advantages such as a high Z element content and high resistivity, **1** exhibits very good prospects in superior efficiency X-ray detection. Consequently, we systematically compared the X-ray attenuation properties of **1** with those of conventional detector materials across a broad energy spectrum (10 keV to 10 MeV) through photon cross-section database analysis (Fig. 3a). **1** exhibited significantly enhanced X-ray absorption compared to Si, reaching performance levels comparable to that of CdTe. Attenuation analysis revealed that a 1 mm thickness of **1** could efficiently attenuate 97.4% of incident X-ray photons, demonstrating exceptional detection suitability (Fig. 3b). In addition, charge collection capability is critical for achieving superior-performance detectors, which can be evaluated using μτ. We fitted the current–voltage ($I$–$V$) curves of **1** and $(I\text{-BA})_2PbI_4$ under X-ray irradiation based on the modified Hecht equation. As shown in Fig. 3c, the calculated value of μτ for **1** was greater than that of $(I\text{-BA})_2PbI_4$. This indicates that the two-dimensional multi-layer structure of **1** has great potential in achieving higher charge collection efficiency.[39] Besides, the polar structure endows **1** with remarkable spontaneous polarization characteristics. The polarization-induced built-in electric field enables **1** to automatically and directionally separate and transport photogenerated carriers, thus exhibiting the bulk photovoltaic effect.[40] Consequently, the self-driven X-ray response of the device under zero-bias conditions was determined. Consistent with predictions, **1** exhibited an obvious radiation-induced photovoltage of 0.15 V under X-ray exposure, establishing a built-in electric field for autonomous charge separation and enabling self-driven X-ray detection (Fig. 3d).

Fig. 4a shows a pronounced enhancement in photo-current density from detector **1** as the X-ray dose rate escalated from

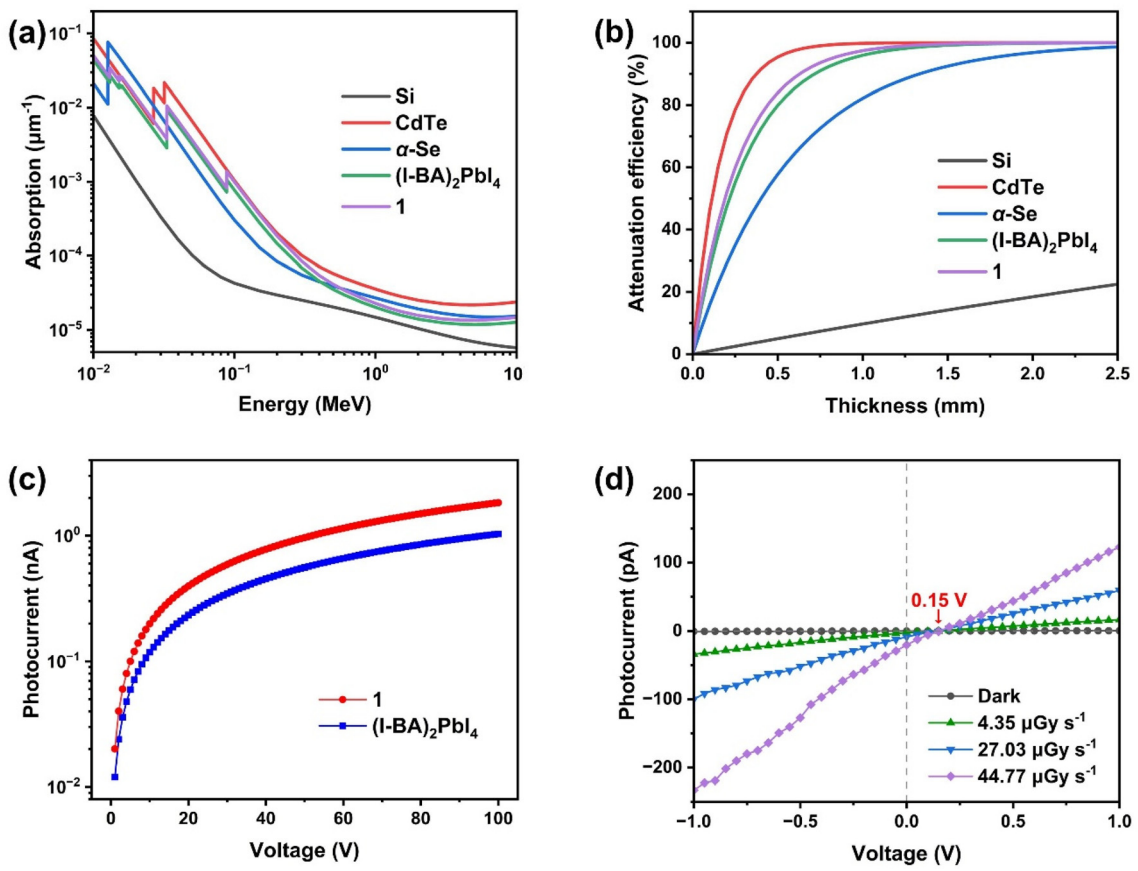


**Fig. 3** (a) The X-ray absorption coefficient of Si, CdTe, α-Se, $(I\text{-BA})_2PbI_4$ and **1**. (b) The attenuation efficiency of Si, CdTe, α-Se, $(I\text{-BA})_2PbI_4$ and **1** at 50 keV photon energy. (c) The mobility-lifetime product of **1** and $(I\text{-BA})_2PbI_4$. (d) $I$–$V$ characteristics of **1** under X-ray illumination.

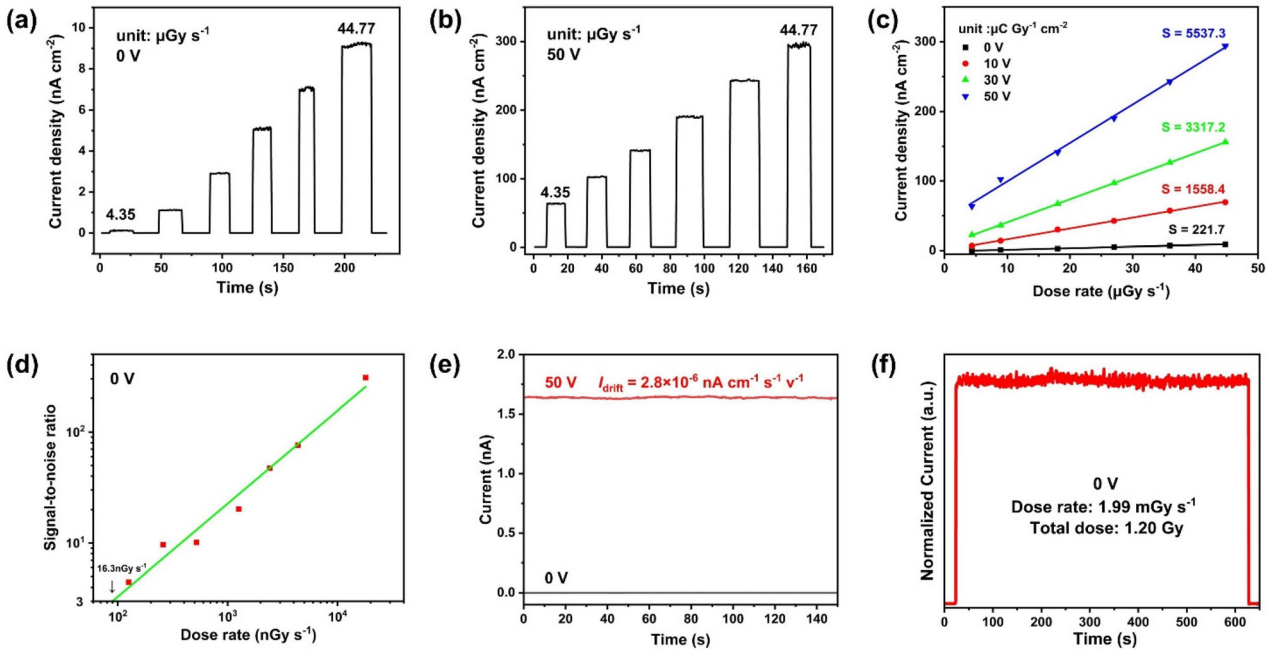


**Fig. 4** (a and b) Current density–time curves for the **1** detector under varying X-ray dose rates at 0 and 50 V bias, respectively. (c) The photocurrent densities at different bias voltages as a function of X-ray dose rates. (d) The SNR of the **1** SC detector under different X-ray dose rates at zero bias indicates an ultra-low LoD of 16.3 nGy $s^{-1}$. (e) The $I_{drift}$ at 0 V and 50 V. (f) The photocurrent response of the **1** SC device during continuous X-ray irradiation.

4.35 to 44.77 μGy $s^{-1}$ under zero-bias conditions, confirming its superior radiation responsiveness. By fitting the current density corresponding to different dose rates at 0 V bias, the measured sensitivity was 221.7 μC $Gy^{-1}$ $cm^{-2}$. This value exceeds those of some reported hybrid perovskites in self-driven mode, such as (*R*-PPA)(IEA)$PbBr_4$ (48.4 μC $Gy^{-1}$ $cm^{-2}$),[41] $(S\text{-BPEA})_2FAPb_2I_7$ (87.8 μC $Gy^{-1}$ $cm^{-2}$)[42] and $(IEA)_2FAPb_2I_7$ (157.6 μC $Gy^{-1}$ $cm^{-2}$).[43] Moreover, as depicted in Fig. 4b and c, owing to enhanced charge extraction with an applied bias, at the same X-ray dose, the photocurrent density of detector **1** gradually increased with the enhancement of the external electric field. When the bias voltage grew from 10 V up to 50 V, the sensitivity rose substantially from 1558.4 μC $Gy^{-1}$ $cm^{-2}$ to 5537.3 μC $Gy^{-1}$ $cm^{-2}$, highlighting its potential in X-ray detection research.[44]

The detection limit is another important parameter for evaluating the performance of X-ray detectors.[45,46] The detection limit is formally defined by the International Union of Pure and Applied Chemistry (IUPAC) as the X-ray dose rate required to yield a signal exceeding noise levels by a factor of three. We recorded the current density–time ($J$–$t$) curve of the device under X-ray irradiation at a lower dose rate (Fig. S8, SI) and calculated the corresponding signal-to-noise ratio. Therefore, the detection limit of **1** at 0 V bias was calculated as shown in Fig. 4d. Significantly, even at the ultra-low dose rate of 125.8 nGy $s^{-1}$, the system maintained an exceptional SNR of 4.46. Quantitative analysis established a LoD of 16.3 nGy $s^{-1}$, outperforming standard medical X-ray requirements (5.5 μGy $s^{-1}$)[47] by a factor of 337. This characteristic is extremely beneficial for practical medical imaging applications and in line with the pursuit of minimizing radiation hazards in the modern medical field. Fig. 4e shows the dark current drift ($I_{drift}$) of detector **1**. Even with a substantial external bias of 50 V applied, the device exhibited a moderate $I_{drift}$ ($2.8 \times 10^{-6}$ nA $cm^{-1}$ $s^{-1}$ $V^{-1}$), particularly given its minimal and extremely stable dark current, which further highlights the merits of the self-driven detection. The detector based on **1** was also exposed to continuous X-ray radiation to evaluate its radiation stability.[48,49] The photocurrent and dark current remained stable under X-ray irradiation with a total accumulated dose of up to 1.20 Gy (Fig. 4f), highlighting its excellent irradiation stability.

## Conclusions

In summary, we reported a multilayer metal halide perovskite with halogenated amines as large spacer cations. The combination of the multilayer structure of the lead iodide inorganic framework and the halogenated amine cations endowed **1** with a polar structure, excellent electrical properties, and a narrow bandgap of 1.72 eV. Specifically, even without a bias voltage, an outstanding responsivity of 35.3 mA $W^{-1}$ and a detectivity of $1.47 \times 10^{12}$ Jones were achieved under illumination at 520 nm. In addition, **1** demonstrated outstanding self-driven X-ray detection capabilities with a high sensitivity of 221.7 μC $Gy^{-1}$ $cm^{-2}$ and a low detection limit of 16.3 nGy $s^{-1}$. All these merits indicate that **1** is a prominent material for high-per-

 

formance self-driven X-ray detection and provide insights into the design of 2D perovskites for self-driven photodetection.

## Author contributions

Haotian Wen: design of the study, data collection and analysis, and writing – original draft. Minmin Wang: data analysis. Xin Dong: data analysis and writing – review & editing. Zhijin Xu: data analysis. Yaru Geng: data analysis. Jie Qin: data analysis. Junhua Luo: resources, project administration, and funding acquisition. Min Zhang: resources and project administration. Lina Li: resources, project administration, writing – review & editing, and supervision.

## Conflicts of interest

There are no conflicts to declare.

## Data availability

The data that support the findings of this study are available from the corresponding author upon reasonable request.

Supplementary information (SI) is available. See DOI: https://doi.org/10.1039/d5qi01912e.

## Acknowledgements

This work was financially supported by NSFC (22322506 and 22175177), the NSF of Fujian Province (2023J06052), the Financial Support of Fujian Province (2023H0043), and the Key Research Program of Frontier Sciences of the Chinese Academy of Sciences (ZDBS-LY-SLH024).

## References

1 R. Zhuang, X. Wang, W. Ma, Y. Wu, X. Chen, L. Tang, H. Zhu, J. Liu, L. Wu, W. Zhou, X. Liu and Y. Yang, Highly sensitive X-ray detector made of layered perovskite-like $(NH_4)_3Bi_2I_9$ single crystal with anisotropic response, *Nat. Photonics*, 2019, **13**, 602–608.

2 X. Geng, Y.-A. Chen, Y.-Y. Li, J. Ren, G.-H. Dun, K. Qin, Z. Lin, J. Peng, H. Tian, Y. Yang, D. Xie and T.-L. Ren, Lead-Free Halide Perovskites for Direct X-Ray Detectors, *Adv. Sci.*, 2023, **10**, 2300256.

3 H. Wu, Y. Ge, G. Niu and J. Tang, Metal Halide Perovskites for X-Ray Detection and Imaging, *Matter*, 2021, **4**, 144–163.

4 Y. He, J. Song, M. Li, K. Sakhatskyi, W. Li, X. Feng, B. Yang, M. Kovalenko and H. Wei, Perovskite computed tomography imager and three-dimensional reconstruction, *Nat. Photonics*, 2024, **18**, 1052–1058.

5 Y. C. Kim, K. H. Kim, D.-Y. Son, D.-N. Jeong, J.-Y. Seo, Y. S. Choi, I. T. Han, S. Y. Lee and N.-G. Park, Printable organometallic perovskite enables large-area, low-dose X-ray imaging, *Nature*, 2017, **550**, 87–91.

6 J. Jiang, M. Xiong, K. Fan, C. Bao, D. Xin, Z. Pan, L. Fei, H. Huang, L. Zhou, K. Yao, X. Zheng, L. Shen and F. Gao, Synergistic strain engineering of perovskite single crystals for highly stable and sensitive X-ray detectors with low-bias imaging and monitoring, *Nat. Photonics*, 2022, **16**, 575–581.

7 W. Pan, H. Wu, J. Luo, Z. Deng, C. Ge, C. Chen, X. Jiang, W.-J. Yin, G. Niu, L. Zhu, L. Yin, Y. Zhou, Q. Xie, X. Ke, M. Sui and J. Tang, $Cs_2AgBiBr_6$ single-crystal X-ray detectors with a low detection limit, *Nat. Photonics*, 2017, **11**, 726–732.

8 W. Guo, X. Liu, S. Han, Y. Liu, Z. Xu, M. Hong, J. Luo and Z. Sun, Room-Temperature Ferroelectric Material Composed of a Two-Dimensional Metal Halide Double Perovskite for X-ray Detection, *Angew. Chem., Int. Ed.*, 2020, **59**, 13879–13884.

9 Y. Shen, Y. Liu, H. Ye, Y. Zheng, Q. Wei, Y. Xia, Y. Chen, K. Zhao, W. Huang and S. Liu, Centimeter-Sized Single Crystal of Two-Dimensional Halide Perovskites Incorporating Straight-Chain Symmetric Diammonium Ion for X-Ray Detection, *Angew. Chem., Int. Ed.*, 2020, **59**, 14896–14902.

10 C. Ma, S. Wang, L. Gao, Z. Xu, X. Song, T. Yang, H. Li, X. Liu, S. Liu and K. Zhao, Halide-Initiated Structural Regulation in Amidino-Based Low-Dimensional Perovskite/Perovskitoid and Their Application for Crystal X-Ray Detectors, *Adv. Opt. Mater.*, 2023, **11**, 2202449.

11 H. Wei, Y. Fang, P. Mulligan, W. Chuirazzi, H.-H. Fang, C. Wang, B. R. Ecker, Y. Gao, M. A. Loi, L. Cao and J. Huang, Sensitive X-ray detectors made of methylammonium lead tribromide perovskite single crystals, *Nat. Photonics*, 2016, **10**, 333–339.

12 P.-J. Huang, K. Taniguchi and H. Miyasaka, Bulk Photovoltaic Effect in a Pair of Chiral–Polar Layered Perovskite-Type Lead Iodides Altered by Chirality of Organic Cations, *J. Am. Chem. Soc.*, 2019, **141**, 14520–14523.

13 C.-K. Yang, W.-N. Chen, Y.-T. Ding, J. Wang, Y. Rao, W.-Q. Liao, Y.-Y. Tang, P.-F. Li, Z.-X. Wang and R.-G. Xiong, The First 2D Homochiral Lead Iodide Perovskite Ferroelectrics: [*R*- and *S*-1-(4-Chlorophenyl) ethylammonium]$_2PbI_4$, *Adv. Mater.*, 2019, **31**, 1808088.

14 S. Shrestha, R. Fischer, G. J. Matt, P. Feldner, T. Michel, A. Osvet, I. Levchuk, B. Merle, S. Golkar, H. Chen, S. F. Tedde, O. Schmidt, R. Hock, M. Rührig, M. Göken, W. Heiss, G. Anton and C. J. Brabec, High-performance direct conversion X-ray detectors based on sintered hybrid lead triiodide perovskite wafers, *Nat. Photonics*, 2017, **11**, 436–440.

15 I.-H. Park, K. C. Kwon, Z. Zhu, X. Wu, R. Li, Q.-H. Xu and K. P. Loh, Self-Powered Photodetector Using Two-Dimensional Ferroelectric Dion–Jacobson Hybrid Perovskites, *J. Am. Chem. Soc.*, 2020, **142**, 18592–18598.

16 Y.-Y. Tang, W.-Y. Zhang, P.-F. Li, H.-Y. Ye, Y.-M. You and R.-G. Xiong, Ultrafast Polarization Switching in a Biaxial

Molecular Ferroelectric Thin Film: [Hdabco]$ClO_4$, *J. Am. Chem. Soc.*, 2016, **138**, 15784–15789.

17 X. Dong, J. Liang, Z. Xu, H. Wu, L. Wang, S. You, J. Luo and L. Li, Exploring centimeter-sized crystals of bismuth-iodide perovskite toward highly sensitive X-ray detection, *Chin. Chem. Lett.*, 2024, **35**, 108708.

18 S. You, Z.-K. Zhu, S. Dai, J. Wu, Q. Guan, T. Zhu, P. Yu, C. Chen, Q. Chen and J. Luo, Inch-Size Single Crystals of Lead-Free Chiral Perovskites with Bulk Photovoltaic Effect for Stable Self-Driven X-Ray Detection, *Adv. Funct. Mater.*, 2023, **33**, 2303523.

19 C.-C. Fan, X.-B. Han, B.-D. Liang, C. Shi, L.-P. Miao, C.-Y. Chai, C.-D. Liu, Q. Ye and W. Zhang, Chiral Rashba Ferroelectrics for Circularly Polarized Light Detection, *Adv. Mater.*, 2022, **34**, 2204119.

20 J. Yan, F. Gao, Y. Tian, Y. Li, W. Gong, S. Wang, H. Zhu and L. Li, Controllable Perovskite Single Crystal Heterojunction for Stable Self-Powered Photo-Imaging and X-Ray Detection, *Adv. Opt. Mater.*, 2022, **10**, 2200449.

21 X. Zhang, T. Zhu, C. Ji, Y. Yao and J. Luo, In Situ Epitaxial Growth of Centimeter-Sized Lead-Free $(BA)_2CsAgBiBr_7$/$Cs_2AgBiBr_6$ Heterocrystals for Self-Driven X-ray Detection, *J. Am. Chem. Soc.*, 2021, **143**, 20802–20810.

22 X. Zhang, L. Li, C. Ji, X. Liu, Q. Li, K. Zhang, Y. Peng, M. Hong and J. Luo, Rational design of high-quality 2D/3D perovskite heterostructure crystals for record-performance polarization-sensitive photodetection, *Natl. Sci. Rev.*, 2021, **8**, nwab044.

23 K. Tao, C. Xiong, J. Lin, D. Ma, S. Lin, B. Wang and H. Li, Self-Powered Photodetector Based on Perovskite/$NiO_x$ Heterostructure for Sensitive Visible Light and X-Ray Detection, *Adv. Electron. Mater.*, 2023, **9**, 2201222.

24 X. Wang, Y. Li, Y. Xu, Y. Pan, C. Zhu, D. Zhu, Y. Wu, G. Li, Q. Zhang, Q. Li, X. Zhang, J. Wu, J. Chen and W. Lei, Solution-Processed Halide Perovskite Single Crystals with Intrinsic Compositional Gradients for X-ray Detection, *Chem. Mater.*, 2020, **32**, 4973–4983.

25 T. Zhu, W. Weng, C. Ji, X. Zhang, H. Ye, Y. Yao, X. Li, J. Li, W. Lin and J. Luo, Chain-to-Layer Dimensionality Engineering of Chiral Hybrid Perovskites to Realize Passive Highly Circular-Polarization-Sensitive Photodetection, *J. Am. Chem. Soc.*, 2022, **144**, 18062–18068.

26 J. Wu, S. You, P. Yu, Q. Guan, Z.-K. Zhu, Z. Li, C. Qu, H. Zhong, L. Li and J. Luo, Chirality Inducing Polar Photovoltage in a 2D Lead-Free Double Perovskite toward Self-Powered X-ray Detection, *ACS Energy Lett.*, 2023, **8**, 2809–2816.

27 T. Schmitt, S. Bourelle, N. Tye, G. Soavi, A. D. Bond, S. Feldmann, B. Traore, C. Katan, J. Even, S. E. Dutton and F. Deschler, Control of Crystal Symmetry Breaking with Halogen-Substituted Benzylammonium in Layered Hybrid Metal-Halide Perovskites, *J. Am. Chem. Soc.*, 2020, **142**, 5060–5067.

28 A. M. Najarian, F. Dinic, H. Chen, R. Sabatini, C. Zheng, A. Lough, T. Maris, M. I. Saidaminov, F. P. García de Arquer, O. Voznyy, S. Hoogland and E. H. Sargent, Homomeric chains of intermolecular bonds scaffold octahedral germanium perovskites, *Nature*, 2023, **620**, 328–335.

29 M. L. Ball, J. V. Milić and Y.-L. Loo, The Emerging Role of Halogen Bonding in Hybrid Perovskite Photovoltaics, *Chem. Mater.*, 2022, **34**, 2495–2502.

30 T. Sheikh, S. Maqbool, P. Mandal and A. Nag, Introducing Intermolecular Cation-π Interactions for Water-Stable Low Dimensional Hybrid Lead Halide Perovskites, *Angew. Chem., Int. Ed.*, 2021, **60**, 18265–18271.

31 Y. Liu, S. Han, J. Wang, Y. Ma, W. Guo, X.-Y. Huang, J.-H. Luo, M. Hong and Z. Sun, Spacer Cation Alloying of a Homoconformational Carboxylate trans Isomer to Boost in-Plane Ferroelectricity in a 2D Hybrid Perovskite, *J. Am. Chem. Soc.*, 2021, **143**, 2130–2137.

32 T. Chen, W. Yang, C. Shi, Z. Xu, X. Dong, J. Liang, J. Luo and L. Li, Mn(II)-Doped Perovskites with Carboxylic Acid Dimers Exhibiting Scintillation, *Inorg. Chem.*, 2025, **64**, 5652–5660.

33 H. Li, W. Jiang, J. Wu, J. Ren, Y. Zhao, D. Liu, Z. Hu and Y. Zhao, Ultralow Ion Migration and X-Ray Response from Strong Dipole Moments in $(Br\text{-}EA)_2PbBr_4$ Perovskite Single Crystals, *Small*, 2025, **21**, 2406722.

34 J. Xue, Y. Huang, Y. Liu, Z. Chen, H. H. Y. Sung, I. D. Williams, Z. Zhu, L. Mao, X. Chen and H. Lu, Rashba Band Splitting and Bulk Photovoltaic Effect Induced by Halogen Bonds in Hybrid Layered Perovskites, *Angew. Chem., Int. Ed.*, 2023, **62**, e202304486.

35 D. Li, W. Wu, S. Han, X. Liu, Y. Peng, X. Li, L. Li, M. Hong and J. Luo, A reduced-dimensional polar hybrid perovskite for self-powered broad-spectrum photodetection, *Chem. Sci.*, 2021, **12**, 3050–3054.

36 C. C. Stoumpos, D. H. Cao, D. J. Clark, J. Young, J. M. Rondinelli, J. I. Jang, J. T. Hupp and M. G. Kanatzidis, Ruddlesden–Popper Hybrid Lead Iodide Perovskite 2D Homologous Semiconductors, *Chem. Mater.*, 2016, **28**, 2852–2867.

37 J. M. Hoffman, C. D. Malliakas, S. Sidhik, I. Hadar, R. McClain, A. D. Mohite and M. G. Kanatzidis, Long periodic ripple in a 2D hybrid halide perovskite structure using branched organic spacers, *Chem. Sci.*, 2020, **11**, 12139–12148.

38 J. M. Hoffman, X. Che, S. Sidhik, X. Li, I. Hadar, J.-C. Blancon, H. Yamaguchi, M. Kepenekian, C. Katan, J. Even, C. C. Stoumpos, A. D. Mohite and M. G. Kanatzidis, From 2D to 1D Electronic Dimensionality in Halide Perovskites with Stepped and Flat Layers Using Propylammonium as a Spacer, *J. Am. Chem. Soc.*, 2019, **141**, 10661–10676.

39 X. Li, J. Hoffman, W. Ke, M. Chen, H. Tsai, W. Nie, A. D. Mohite, M. Kepenekian, C. Katan, J. Even, M. R. Wasielewski, C. C. Stoumpos and M. G. Kanatzidis, Two-Dimensional Halide Perovskites Incorporating Straight Chain Symmetric Diammonium Ions, $(NH_3C_mH_{2m}NH_3)(CH_3NH_3)_{n-1}Pb_nI_{3n+1}$ (m = 4–9; n = 1–4), *J. Am. Chem. Soc.*, 2018, **140**, 12226–12238.

40 L. Guo, X. Liu, L. Gao, X. Wang, L. Zhao, W. Zhang, S. Wang, C. Pan and Z. Yang, Ferro-Pyro-Phototronic Effect

 

in Monocrystalline 2D Ferroelectric Perovskite for High-Sensitive, Self-Powered, and Stable Ultraviolet Photodetector, *ACS Nano*, 2022, **16**, 1280–1290.

41 Z.-K. Zhu, J. Wu, P. Yu, Y. Zeng, R. Li, Q. Guan, H. Dai, G. Chen, H. Yang, X. Liu, L. Li, C. Ji and J. Luo, Polar Alternating Cations Intercalated Hybrid Perovskite with Iodine-Substituted Spacers Toward Efficient Passive X-Ray Detection, *Adv. Funct. Mater.*, 2024, **34**, 2409857.

42 Q. Guan, H. Ye, S. You, Z.-K. Zhu, H. Li, X. Liu and J. Luo, Radiation Photovoltaics in a 2D Multilayered Chiral-Polar Halide Perovskite toward Efficient Self-Driven X-Ray Detection, *Small*, 2024, **20**, 2307908.

43 D. Fu, Y. Zhang, Z. Chen, L. Pan, Y. He and J. Luo, Bulk Photovoltaic Effect Induced by Non-Covalent Interactions in Bilayered Hybrid Perovskite for Efficient Passive X-Ray Detection, *Small*, 2024, **20**, 2403198.

44 W. Pan, W. Li, J. Zong, H. Hu, K. Guo, C. Li, W. Qu and H. Wei, A Low-Dimensional Donor-Acceptor Perovskite for High-Performance X-Ray Detection, *Adv. Funct. Mater.*, 2025, **35**, 2414553.

45 Y. Liu, Z. Xu, Z. Yang, Y. Zhang, J. Cui, Y. He, H. Ye, K. Zhao, H. Sun, R. Lu, M. Liu, M. G. Kanatzidis and S. Liu, Inch-Size 0D-Structured Lead-Free Perovskite Single Crystals for Highly Sensitive Stable X-Ray Imaging, *Matter*, 2020, **3**, 180–196.

46 A. Glushkova, P. Andričević, R. Smajda, B. Náfrádi, M. Kollár, V. Djokić, A. Arakcheeva, L. Forró, R. Pugin and E. Horváth, Ultrasensitive 3D Aerosol-Jet-Printed Perovskite X-ray Photodetector, *ACS Nano*, 2021, **15**, 4077–4084.

47 Y. Zhang, Y. Liu, Z. Xu, H. Ye, Z. Yang, J. You, M. Liu, Y. He, M. G. Kanatzidis and S. Liu, Nucleation-controlled growth of superior lead-free perovskite $Cs_3Bi_2I_9$ single-crystals for high-performance X-ray detection, *Nat. Commun.*, 2020, **11**, 2304.

48 X. Feng, L. Zhang, X. Feng, J. You, J. Pi, H. Zeng, D. Chu, C. Xue, K. Zhao, S. Jia, P. Tong, Z. Jin, Y. Liu, A. K. Y. Jen and S. F. Liu, Ion Migration Suppression via Doping Multivalent Cations in Perovskite for High Thermal Stability X-ray Detectors, *ACS Energy Lett.*, 2025, **10**, 685–695.

49 X. Zheng, W. Zhao, P. Wang, H. Tan, M. I. Saidaminov, S. Tie, L. Chen, Y. Peng, J. Long and W.-H. Zhang, Ultrasensitive and stable X-ray detection using zero-dimensional lead-free perovskites, *J. Energy Chem.*, 2020, **49**, 299–306.